Performance of a focused 2D anti-scatter grid for industrial X-ray computed tomography

Joseph John Lifton[1]*, Zheng Jie Tan[2], Christian Filemon[3]

[1] Mechanical Engineering Department, Faculty of Engineering and Physical Sciences, University of Southampton, SO17 1BJ, UK

[2] Advanced Remanufacturing & Technology Centre (ARTC), Agency for Science, Technology and Research (A*STAR), 3 CleanTech Loop, #01-01 CleanTech Two, Singapore, 637143, Republic of Singapore

[3] School of Mechanical and Aerospace Engineering, Nanyang Technological University, 50 Nanyang Ave, Singapore, 639798, Republic of Singapore

*J.J.Lifton@soton.ac.uk

Abstract

X-ray computed tomography (XCT) is increasingly being used for the measurement and inspection of large dense metallic engineering components. When scanning such components, the quality of the data is degraded by the presence of scattered radiation. In this work, the performance of a focused 2D anti-scatter grid (ASG) is investigated for scanning samples made from cobalt chrome and Inconel on a 450 kV cone-beam XCT system. The devised scatter correction method requires one additional scan of the sample, and for projections to be algorithmically processed prior to reconstruction. The results show that the ASG based scatter correction method increases the contrast-to-noise of the data by 14.5% and 61.5% for the cobalt chrome and Inconel samples, respectively. Furthermore, the method increases edge sharpness by 6% and 16.9% for outer and inner edges, respectively.

1 Introduction

Cone beam X-ray computed tomography (XCT) has become an indispensable tool for non-destructive inspection and dimensional measurement in high-value engineering. Micro-focus XCT systems with acceleration voltages of 225 to 300 kV are now commonplace in research and development labs, as well as production facilities; however, the ability of these systems to scan metallic engineering components is very limited, as only a few millimetres of steel can be penetrated at these X-ray energies [1]. Higher energy micro- to milli-focus XCT systems with acceleration voltages of 450 to 600 kV enable larger steel and nickel alloy components to be scanned, however, as X-ray energy increases, the dominant X-ray-matter interaction becomes Compton scattering, which is detrimental to the quality of attenuation-based computed tomography.

Scattered X-rays are X-rays that have deviated from their incident ray-path as a consequence of undergoing a scattering interaction with either the object being scanned or structures within the X-ray cabinet. X-rays that have not undergone a scattering interaction are termed primary X-rays. The signal detected by an X-ray detector is composed of both scattered and primary X-rays. Fourier-based tomographic reconstruction algorithms assume that the detected signal is composed of primary X-rays only, so the presence of scattered X-rays leads to errors in the reconstruction, these errors typically appear as cupping artefacts, streaking artefacts, and a loss of contrast that can obscure fine details such as cracks and voids and blur material boundaries [2].

Perhaps the most widespread approach to reducing scatter in high energy XCT systems is through the use of a fan-beam scan strategy, whereby the X-ray source is collimated to a fan, and the flat panel detector is replaced by a linear detector that is also collimated. Collimating the source to a fan-beam reduces the amount of scatter generated by the object, whist detector collimation reduces the amount of scatter that reaches the detector. The obvious disadvantage of a fan-beam scan is the increased scan time; a scan that takes hours for a cone-beam configuration may take days for a fan-beam configuration. A scan time of days is not practical in production environments; evidently there is a need for a scatter reduction method for high energy XCT that does not lead to impractical scan times, this being the motivation for the present work.

Scatter correction has been a topic of research since the early days of medical radiography [3]. Most research has focused on medical imaging applications, but scatter is perhaps more problematic for industrial XCT where higher density objects are scanned and X-ray energies are higher, both of which lead to increased scatter signals. The basic approach for scatter correction is to somehow estimate the scatter signal for each projection and then subtract it from the projection prior to reconstruction. Many different methods for estimating scatter signals exist, including: simulating scatter signals using a Monte Carlo [4] or deterministic approach [5], approximating scatter signals as a point spread function [6], measuring scatter signals using beam blockers [7], separating scatter and primary signals in the frequency domain by using a beam modulation pattern [8], and using convolutional neural networks (CNN) to predict scatter signals from scan data [9].

The disadvantages of these approaches are as follows: the simulation approach requires an accurate model of the object being scanned and the XCT system being used, this information is not always available, and it takes considerable effort to achieve agreement between simulation and experiment. Additionally, to accurately match the orientation of the scanned object and the simulated object requires precise fixturing to be designed and fabricated for each new component, this is often impractical due to fabrication lead times as well as the need to then include the fixturing in the simulation. The point spread function approach requires a new point spread function to be generated for each new material and scan setting used, this is not practical for a high-mix, low-volume scan environments and situations where the detailed composition of the object is unknown. Measuring scatter signals using beam blockers is a versatile approach that does not require detailed knowledge of the scanned object. However, beam blockers need to be spaced sparsely to avoid blocking too much of the X-ray beam, otherwise the scatter estimate will be underestimated. Using sparsely spaced blockers leads to only a few scatter sample points in each projection, the missing data must be interpolated which can lead to errors in the scatter estimate [10]. To avoid excessive interpolation, additional beam blocker measurements are acquired by shifting the array in additional scans [10]. A moving blocker approach can be used to avoid additional scans [11] but requires the blocked primary signal to be interpolated, which introduces its own set of errors. Modulation-based scatter correction does not require an additional scan but does require a thin, dense modulation grid to separate primary and scattered radiation in the frequency domain. The modulation approach has only been

demonstrated at medical scanning energies (120 kV) [8] and the digital filters used can introduce filter ringing artifacts [2]; developing a modulation grid for high energies may be challenging as the modulator needs to be generate a strong modulation pattern without changing the X-ray beam energy spectrum. Using a CNN to predict scatter signals based on measured projections requires the CNN to be trained, this requires a significant number of training data sets (16,416 simulated projections were used in [8]), which in turn either requires a very accurate simulation tool, or for scatter signals to be measured using one of the aforementioned methods. Nevertheless, once trained, using a CNN to predict scatter signals from measured projections for subsequent subtraction is an appealing solution since it is fast, requires no human defined parameters, and no additional scanning.

Rather than estimate and subtract scatter signals, another approach is to reduce the amount of scatter incident on a flat panel detector. One simple way to do this is to increase the distance between the object and the detector, termed the air-gap method, this leads to only smaller angle scattering reaching the detector, whilst wider angle scattering misses the detector entirely. Another approach to reduce scatter signals is to use an anti-scatter grid (ASG); an ASG is a device placed between the scanned object and the detector, focused ASGs have an array of high aspect ratio strips of material (septa) that are aligned with the X-ray beam; any X-rays that fall incident on the ASG that are not aligned with the septa (scattered X-rays) will be attenuated. A 1D ASG has septa that are aligned with either the rows or columns of a flat panel detector, while a 2D ASG has two sets of septa that are perpendicular to each other, one parallel with detector rows and the other aligned with detector columns. The main disadvantage of ASGs is that the septa block some primary X-rays, this results in a grid pattern being superimposed on the acquired X-ray images; the removal of these grid artefacts is still an active field of research [12].

There is renewed interest in using ASGs for medical XCT due to additive manufacturing becoming a viable method for manufacturing 2D focused grids from high density materials like tungsten [13, 14, 15] and cobalt chrome [16, 17]. Additive manufacturing allows 2D focused ASGs to be fabricated without the need for the use of septa supporting material, which causes primary X-rays to be absorbed and scattered. The use of ASGs in high energy industrial XCT has been very limited [18, 19], we assume due to the difficulties associated with fabricating ASGs of sufficient size and sufficiently thin septa; typical flat panel detectors are 400 by 400 mm in size, with pixel pitches of 0.2 mm, septa thicknesses should ideally be smaller than the pixel pitch to reduce grid artefacts.

Given the lack of research on the use of ASGs for high energy XCT, the aim of this work is to adopt the ASG scatter reduction approaches demonstrated in the medical CT domain and test their suitability for high energy industrial XCT. This is achieved by fabricating a tungsten 2D focused ASG using additive manufacturing, and devising a scatter correction method that avoids grid artefacts and does not lead to impractical scan times.

2 Methodology

2.1 Anti-scatter grid

A 2D focused ASG is fabricated from EOS Tungsten W1 powder using an EOS M 290 FDR dual-laser laser powder bed fusion 3D printer. The fine-detailed resolution version of the EOS M 290 was used as the smaller laser spot allows the ASG to have half the minimum wall thickness compared to a typical EOS M 290 system. The ASG has a base size of 70 by 70 mm, and a height of 30 mm, the septa have a wall thickness of 0.1 mm and a spacing of 2 mm, this gives a grid ratio of 15:1. The septa are focused, based on an X-ray source to detector distance of 1011.53 mm. A photograph of the ASG is shown in Figure 1.

Tungsten is a high-density metal which makes it suitable for blocking 450 kV X-rays. Additive manufacturing allows the complex geometry of the ASG to be fabricated in a single step, avoiding the need for complicated and time-consuming assembly. The septa wall thickness is chosen to be the smallest wall thickness the fabrication process allows, whist the spacing of the septa is selected based on similar designs found in the literature [13, 14, 15]. The base size of the ASG is limited by the area within the 3D printer that can be scanned by a single laser (125mm by 250 mm). The use of the second laser in the 3D printer was avoided as the stitching error between the two lasers is challenging for creating a single long septa without breakage. The height of the ASG is chosen to fully attenuate 450 kV X-rays that are perfectly aligned with the focused septa.

The ASG is mounted directly in front of the detector by means of a polymer mounting assembly. The mounting assembly allows the ASG to be independently translated in two orthogonal axes, a further rotation axis is positioned on top of the two translational axes, these axes allow the ASG to be precisely aligned with the X-ray cone beam by means of positioning screws. A photograph of the ASG mounted in the XCT system is shown in Figure 2.

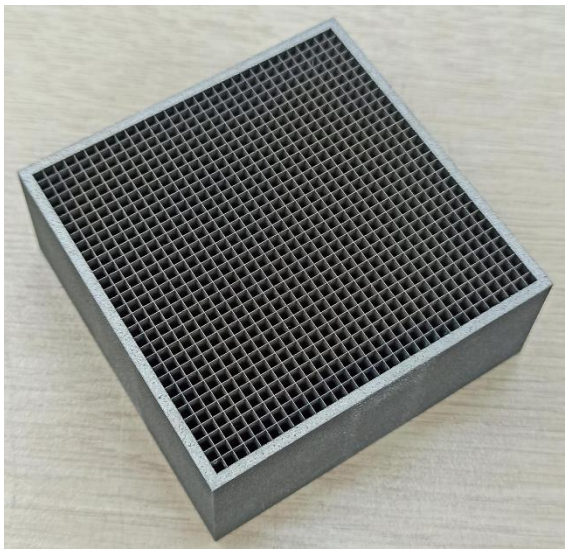

Figure 1: Additively manufactured tungsten 2D focused ASG.

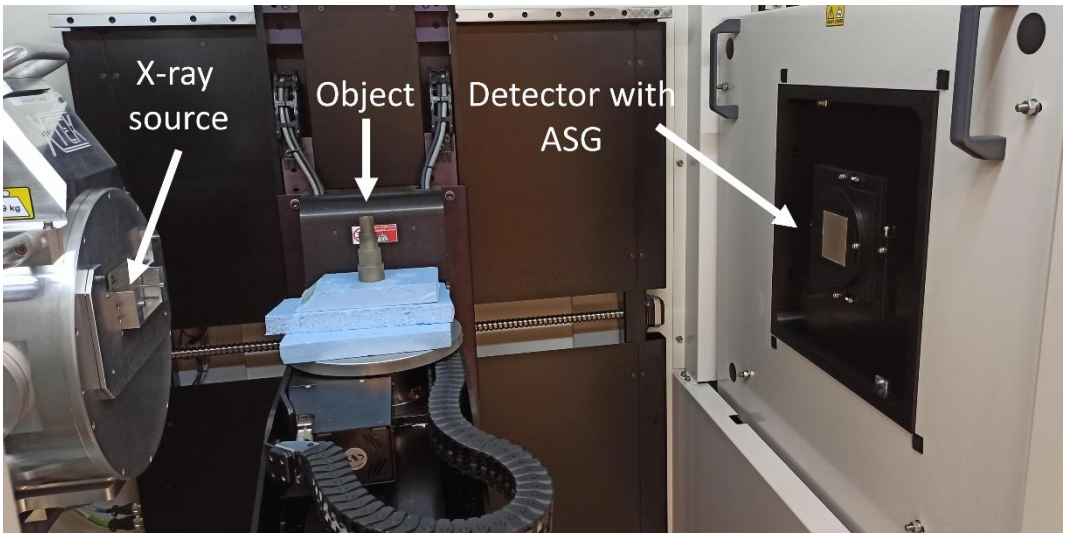

Figure 2: Mounting of the ASG in the XCT system.

2.2 Detector glare correction

Initial experimentation with the ASG shows that the detector signal in the shadow of the septa and the frame of the ASG is not zero; if the frame or septa fully attenuated incident X-rays, then the signal in their shadow should be zero (no X-rays detected). Figure 3a shows a typical X-ray image of an object with the ASG in place, Figure 3b shows the intensity profile drawn across the central row of the detector. It can be seen that the signal in the shadow of the septa closely follows the signal in the unblocked region. When the unblocked signal is high, the blocked signal is high, when the unblocked signal is low, the blocked signal is low. Note that the septa thickness is 0.1 mm and the pixel size is 0.2 mm, so the septa covers half of a pixel when perfectly aligned, we would therefore expect this behaviour since some primary radiation reaches the pixels in the septa shadows. However, the signal in the shadow of the ASG frame is also not zero, see the first and last dip in intensity in Figure 3b; the frame is 2 mm thick so it covers 10 pixels, these pixels should have an intensity of zero given that there is 30 mm of tungsten in front of them.

We attribute the signal in the shadow of the frame to veiling glare [20], this being the scattering of optical photons within the scintillator of the detector, an illustration of this is given in Figure 4. X-rays incident on the scintillator are converted to optical photons that spread out and spill over into neighbouring pixels.

We estimate the relationship between the intensity of the blocked and unblocked pixels by acquiring X-ray images of the ASG with different thicknesses of X-ray beam filter; the blocked region being the pixels in the shadow of the ASG frame. Line profiles across these X-ray images are shown in Figure 3c, as the beam filter thickness increases the intensity of both the unblocked and blocked regions decreases. The beam filters used are: no filter, 2 mm Sn, 4 mm Sn, 4 mm Sn + 2 mm Cu, 4 mm Sn + 4 mm Cu, 4 mm Sn + 6 mm Cu. By sampling the average intensity of blocked and unblocked pixels and plotting one against the other, a linear relationship between the two is found, see Figure 3d. This allows us to estimate the glare signal from the unblocked regions of the X-ray image; this will be used in our scatter correction method in the next section.

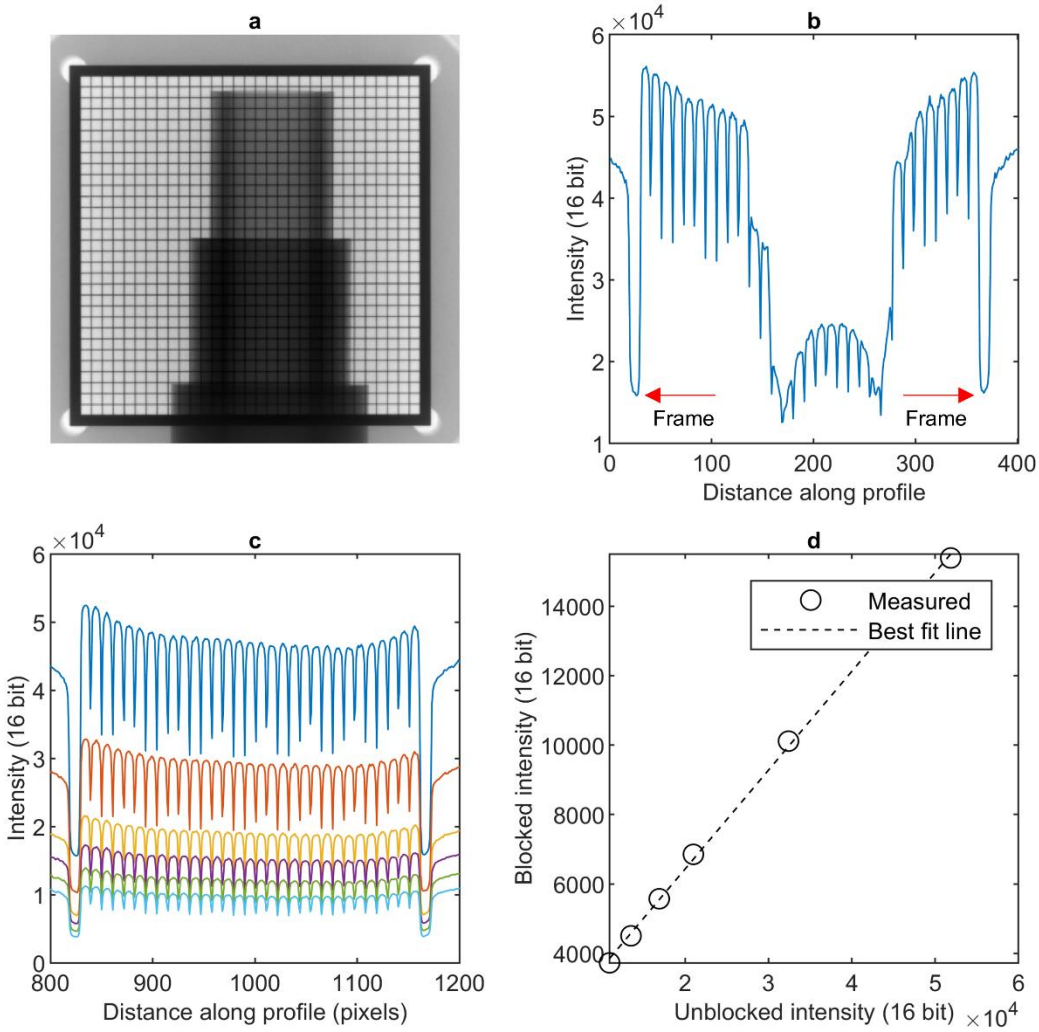

Figure 3: a) X-ray image with object and ASG. b) Line profile across (a) showing how the signal in the shadow of the ASG follows the intensity of the unblocked regions. c) Line profiles across X-ray images of the ASG with increasing amounts of X-ray beam thickness: no filter, 2 mm Sn, 4 mm Sn, 4 mm Sn + 2 mm Cu, 4 mm Sn + 4 mm Cu, 4 mm Sn + 6 mm Cu. d) Relationship between intensity in the blocked regions of the ASG and unblocked regions.

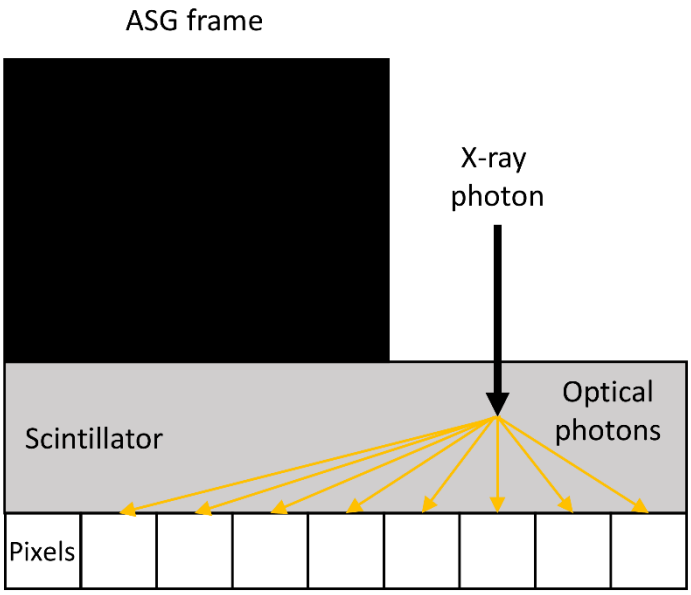

Figure 4: Illustration of veiling glare causing a signal in the shadow of the ASG septa.

2.3 Scatter correction

The proposed scatter correction method is based on the following assumptions: X-ray images are composed of a primary signal, a scattered signal, and a glare signal; X-ray images with the ASG in place are composed of a primary signal and a glare signal, the scatter signal is attenuated by the ASG. We can therefore use a scan of the sample with and without the ASG to isolate the primary signal for subsequent scatter-free reconstruction.

Let the intensity image with the anti-scatter grid in place be I_G, this image is composed of primary X-rays P_G and the detector glare signal G_G.

$$I_G = P_G + G_G \tag{1}$$

Let the intensity image with no anti-scatter grid be I, this image is composed of primary X-rays P, scattered X-rays S, and the detector glare signal G.

$$I = P + S + G \tag{2}$$

From the previous section, the glare signal in I_G is found to be a linear function of I_G:

$$G'_G = m \cdot I_G + c \tag{3}$$

Where $G'_G \approx G_G$, m and c are the gradient and intercept of the best fit line in Figure 3d.

The glare signal is estimated from I_G, and then subtracted to give the primary signal P_G:

$$P_G = I_G - G'_G \tag{4}$$

Note that we cannot directly use the primary signal P_G because it is incomplete due to regions of the image being blocked by the anti-scatter grid, we instead assume that P_G is a good approximation of P.

$$P_G \approx P \tag{5}$$

We can use P_G to estimate the scatter and glare signals in I:

$$S + G = I - P_G \tag{6}$$

With estimates of $S + G$ we can finally estimate P:

$$P = I - S - G \tag{7}$$

A graphical explanation of the processing steps is shown in Figure 5.

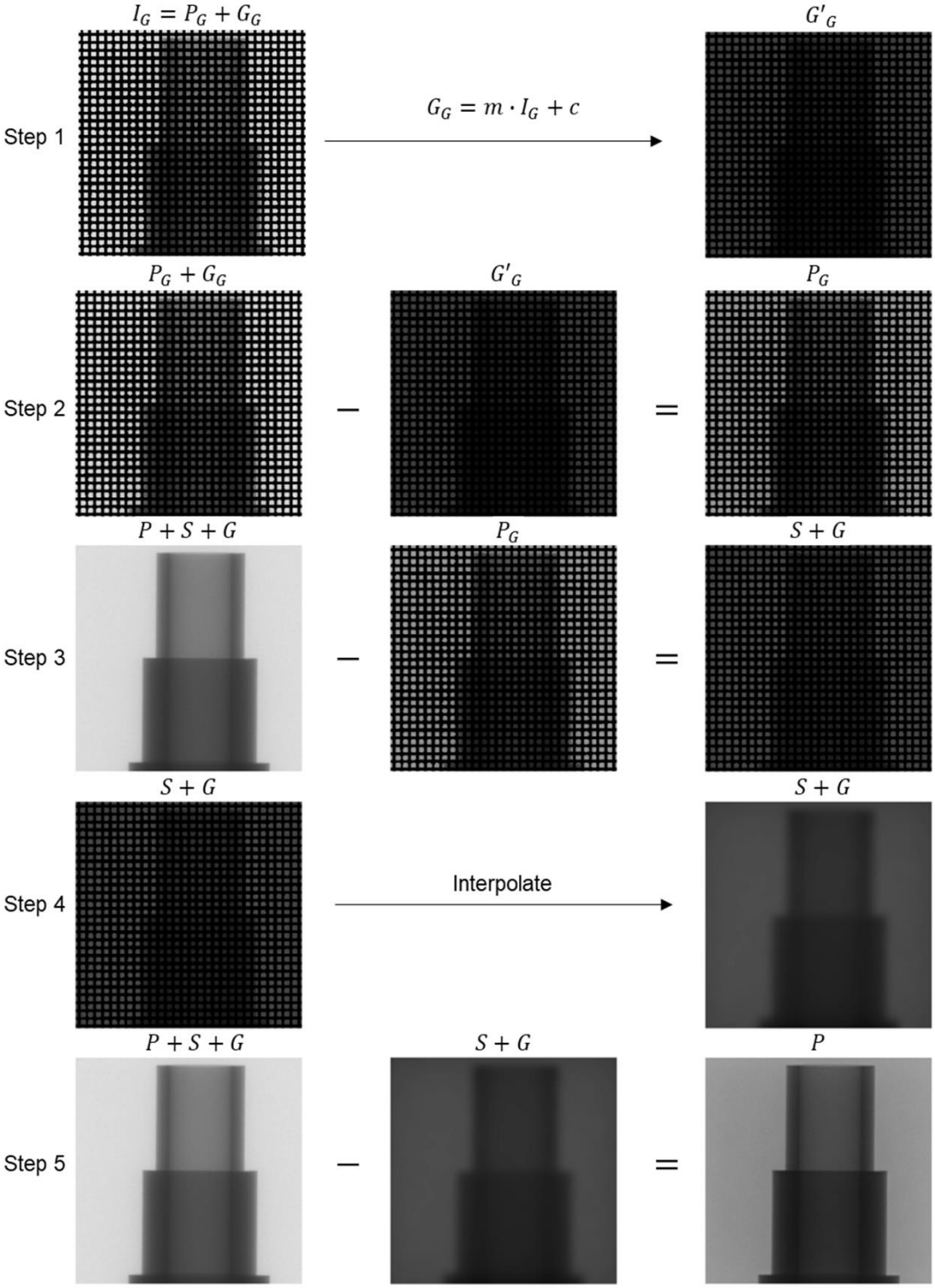

Figure 5: Graphical explanation of the scatter correction method.

2.4 Test samples

To demonstrate the proposed scatter correction method and evaluate its performance, two test samples are scanned, see Figure 6. The first sample is a cobalt chrome (EOS MP1) stepped cylinder, the second is a more complex component with intricate internal channels fabricated from Inconel (EOS NickelAlloy IN718); both samples are fabricated using additive manufacturing. The outer diameters of the top two steps of the cobalt chrome cylinder are 15 mm and 20 mm, the inner diameter is 10 mm. The samples are both fabricated from high density metals; when XCT scanning such metals, the scan data is typically contaminated by scatter, leading to low contrast data that is difficult to visually inspect for manufacturing defects and difficult to segment for quantitative analysis such as porosity measurement and dimensional measurement.

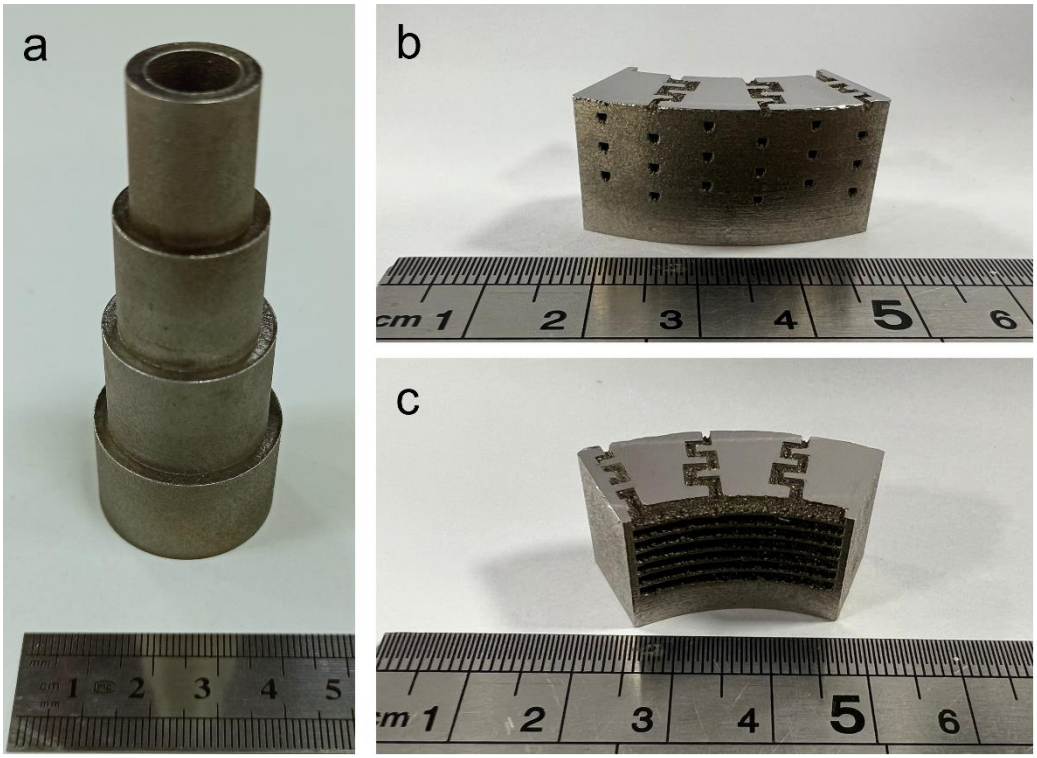

Figure 6: a) Cobalt chrome stepped cylinder, the external diameters of the top two steps are 15 mm and 20 mm, and the internal diameter is 10 mm. b) front view of an Inconel sample with internal channels. c) back view of the Inconel sample.

2.5 XCT scanning and data processing

All scans are conducted on a Nikon XT H 450 kV XCT system; this is a cone beam XCT system with a 450 kV tungsten target X-ray source, and a 400 by 400 mm flat panel detector with 2000 by 2000 pixels (0.2 mm pixel size).

The scan settings for each sample are given in Table 1. Each sample is first scanned without the ASG in place, once the scan is completed the ASG is inserted and the scan is repeated, all the scan settings remain the same for both scans. The detector gain and offset are calculated at the beginning of the first scan, without the ASG in place, the detector settings remain unchanged throughout the subsequent ASG scan. Ring artefact correction is not used as it may influence the results assessing the performance of the ASG.

Once scanning is complete, the projections are processed to correct for scatter as per Figure 5, this is achieved using a computer program written in Matlab 2023a (The MathWorks, Inc., Natick, MA, USA). The first step of the algorithm is to remove the regions of the projections that are blocked by the ASG in the projection set I_G, this is achieved by thresholding a bright field image of the ASG and creating a binary mask with 0 values in the blocked regions and 1 in the unblocked regions. This mask is multiplied with the I_G projection set, followed by the processing steps shown in Figure 5.

Each projection takes approximately 0.2 seconds to process on a laptop with a i5 1345U processor, this amounts to approximately 144 seconds for 720 projections and includes reading and writing the projection images.

Once processed, the corrected and uncorrected projections are reconstructed using an in-house implementation of the FDK filtered backprojection reconstruction algorithm. A Hann filter is used for the filtering step in reconstruction, and linear interpolation is used during backprojection. The data is reconstructed as 32-bit floating-point numbers and is not converted to unsigned integers in order to avoid artificial scaling of the grey values.

Table 1: Scan settings for the two test samples.

	Cobalt chrome stepped cylinder	Inconel test sample with internal channels
Acceleration voltage (kV)	400	430
Filament current (µA)	200	225
Beam filter	4 mm Sn	4 mm Sn
Exposure time (s)	1.4	1.4
Frames per projection	2	2
Number of projections	1080	720
Voxel size (µm)	140	115
Geometric magnification	1.74	1.42

2.6 Image quality metrics

To quantitatively compare the image quality of the XCT data before and after scatter correction, we evaluate the contrast-to-noise ratio (CNR) of the data. This metric is chosen because it is desirable to maximise contrast and minimise noise, doing so will facilitate qualitative and quantitative analysis of the XCT data. The CNR is calculated as:

$$C_{NR} = \frac{\mu_m - \mu_a}{\sqrt{\sigma_m^2 + \sigma_a^2}} \tag{8}$$

Where μ_m is the mean material grey value, μ_a is the mean air grey value, σ_m is the standard deviation of the material grey values, and σ_a is the standard deviation of the air grey values. These terms are sampled from the material and air regions from selected CT slices. The regions are selected by thresholding the CT images into material only regions and air only regions using the automatic thresholding function in imageJ [21].

Scatter correction is expected to lead to sharper edges in XCT data, we therefore compare edge sharpness before and after scatter correction. To do this, line profiles are drawn across the outer and inner edges of the cobalt chrome cylinder, this represents the edge response function, the first derivative of which is the line response function (LRF) [22]. Upon normalising the maximum value of the LRF, the spread of the LRF can be used as a measure of edge sharpness, a larger spread indicates a

lower sharpness, while a smaller spread indicates a higher edge sharpness. We quantify the spread of the LRF by fitting a Gaussian function and evaluating the standard deviation of the fitted Gaussian.

3 Results

CT slices of the cobalt chrome stepped cylinder are shown in Figure 7 with and without scatter correction. The images are plotted with the same grey value range to facilitate a visual comparison of the data. The scatter corrected slices clearly have a higher contrast, but also appear to have more pronounced cupping artefacts; notice the brighter outer edge of the cylinders. Line profiles drawn across the centre of the CT slices are shown in Figure 8a and b, these show the change in contrast and cupping more clearly. The values used to calculate the CNR of the cobalt chrome stepped cylinder are given in Table 2; as a consequence of scatter correction, the CNR of the data increases by 14.5%. Table 2 shows that although the contrast of the data increases $(\mu_m - \mu_a)$, the standard deviation of the material grey values also increases, this being a well-known feature of scatter correction: attenuating the low spatial-frequency scatter signal leads to a greater weighting of the high-spatial frequencies, similar to a high-pass filter.

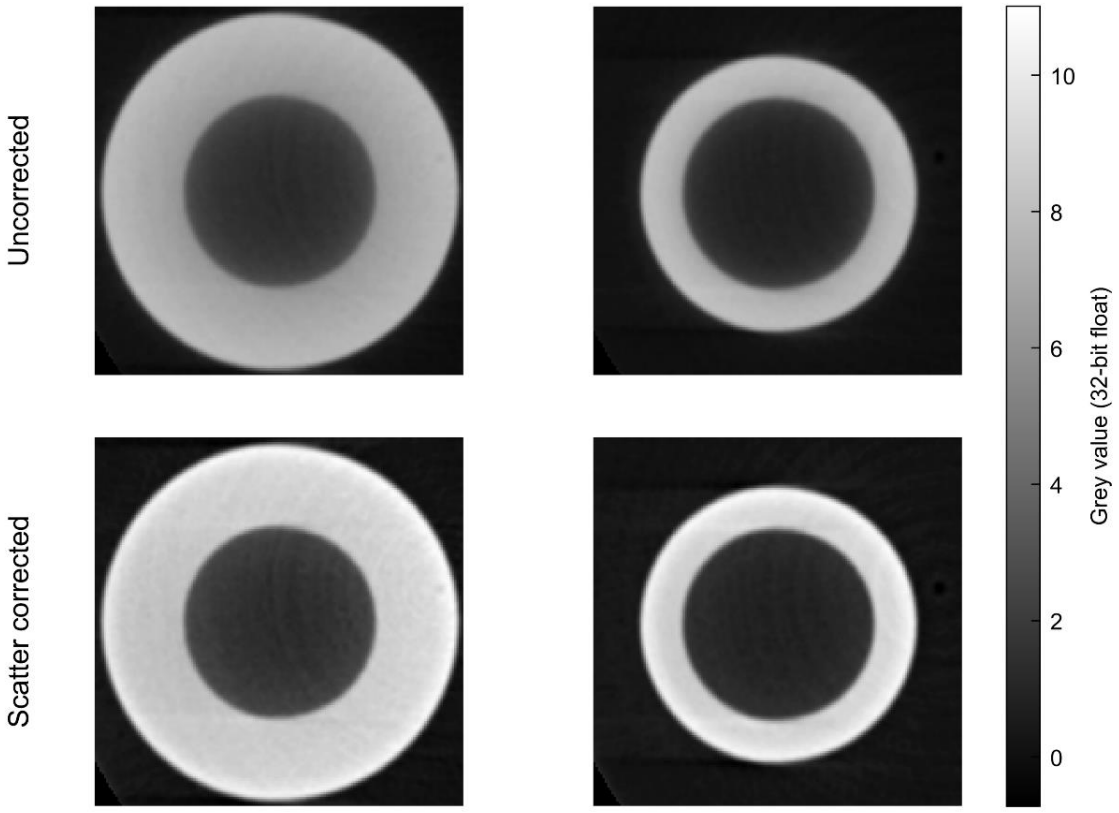

Figure 7: CT images of the cobalt chrome stepped cylinder with and without scatter correction. Left 5 mm wall thickness, right 2.5 mm wall thickness.

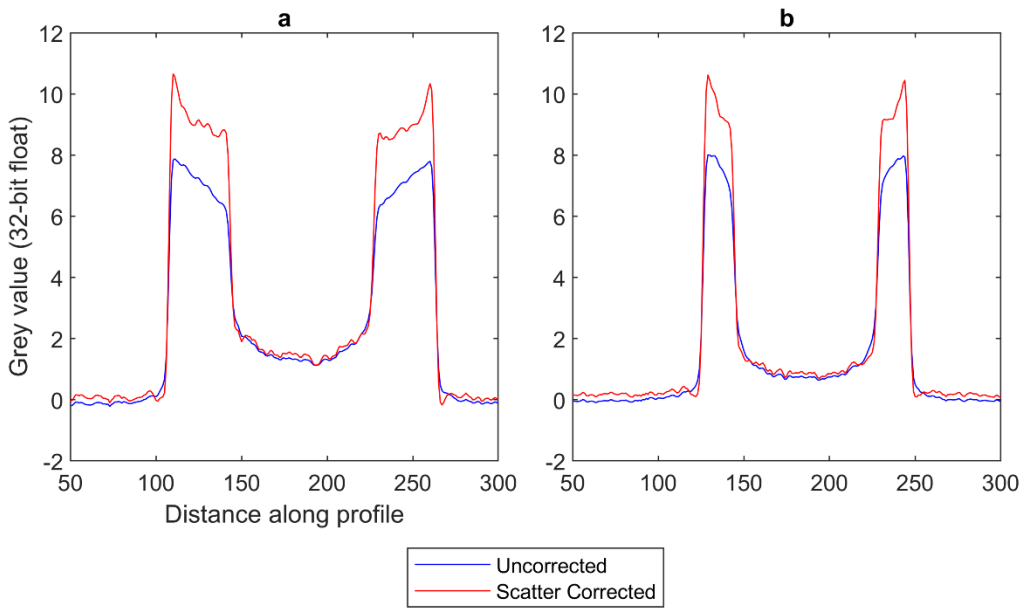

Figure 8: Line profiles drawn across the centre of the CT slices shown in Figure 7. a) Line profiles for the 5 mm wall thickness. b) Line profiles for the 2.5 mm wall thickness.

Table 2: The contrast-to-noise-ratio of the cobalt chrome stepped cylinder, before and after scatter correction.

	μ_m	μ_a	σ_m	σ_a	C_{NR}
Uncorrected	7.13	1.69	0.53	0.33	8.73
Scatter corrected	9.02	1.75	0.66	0.30	9.99
% difference					14.5%

CT slices of the Inconel sample are shown in Figure 9 with and without scatter correction. The images are plotted with the same grey value range to facilitate a visual comparison of the data; the scatter corrected slice clearly has a higher contrast. Line profiles drawn across the centre of the CT slices are shown in Figure 10, these show the change in contrast more clearly. The values used to calculate the CNR of the Inconel sample are given in Table 3; as a consequence of scatter correction, the CNR of the data increases by 61.5%. Table 3 shows that scatter correction has the undesirable effect of increasing both the standard deviation of the material grey values and the air grey values, but this is negated by the significant increase in contrast.

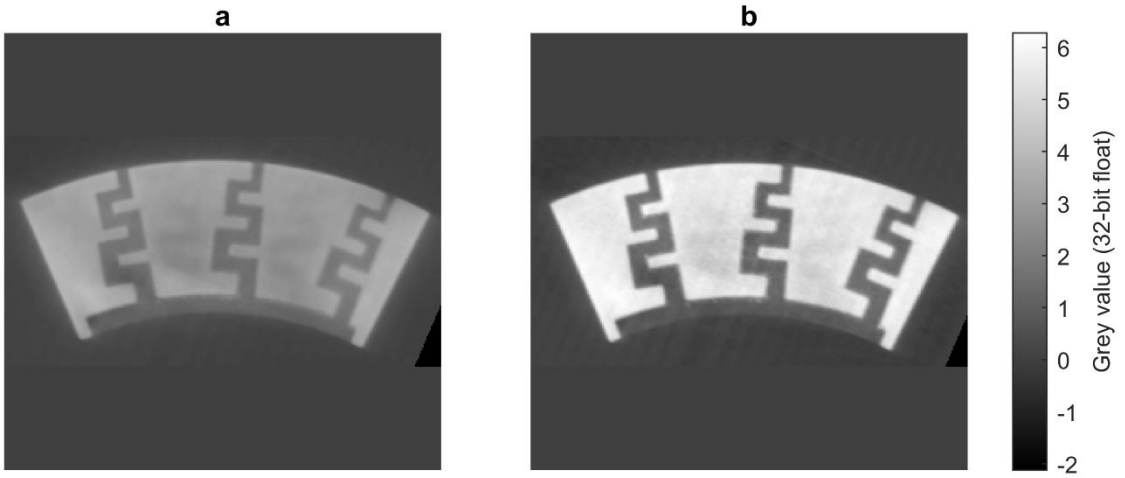

Figure 9: CT slices of the Inconel sample with internal channels. a) without scatter correction, b) with scatter correction.

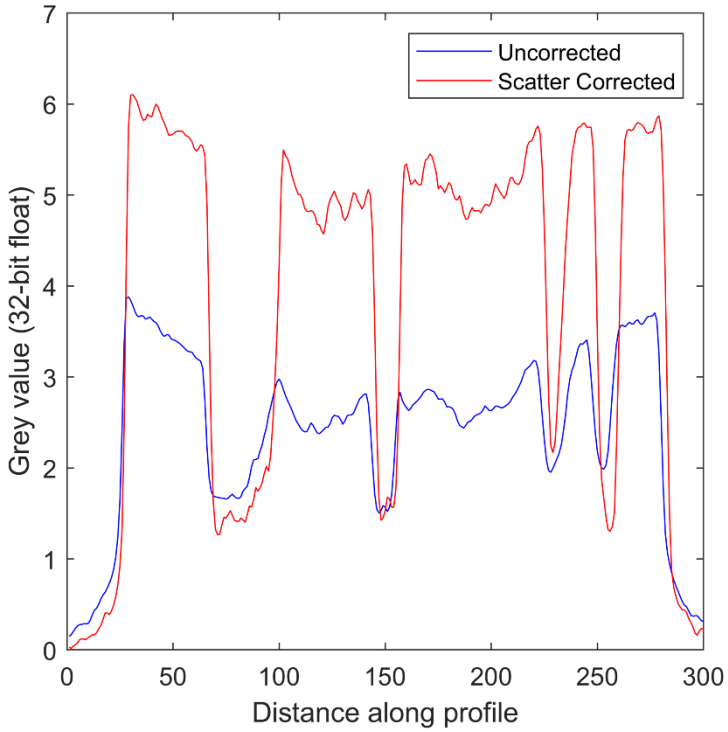

Figure 10: Line profiles drawn across the CT slices in Figure 9.

Table 3: The contrast-to-noise-ratio of the Inconel sample with internal channels, before and after scatter correction.

	μ_m	μ_a	σ_m	σ_a	C_{NR}
Uncorrected	3.04	0.60	0.39	0.67	3.15
Scatter corrected	5.26	0.48	0.63	0.70	5.08
% difference					61.5%

A comparison of the edge sharpness before and after scatter correction is shown in Figure 11, for the inner and outer edges of the cobalt chrome sample. The standard deviation of the outer edge is 2.15 pixels without scatter correction and 2.02 pixels with scatter correction: scatter correction leads to a 6% improvement in edge sharpness. The standard deviation of the inner edge is 2.66 pixels without scatter correction and 2.21 pixels with scatter correction: a 16.9% improvement in edge sharpness. Scatter correction has the desirable effect of improving edge sharpness for both internal and external edges, with a greater effect for internal edges.

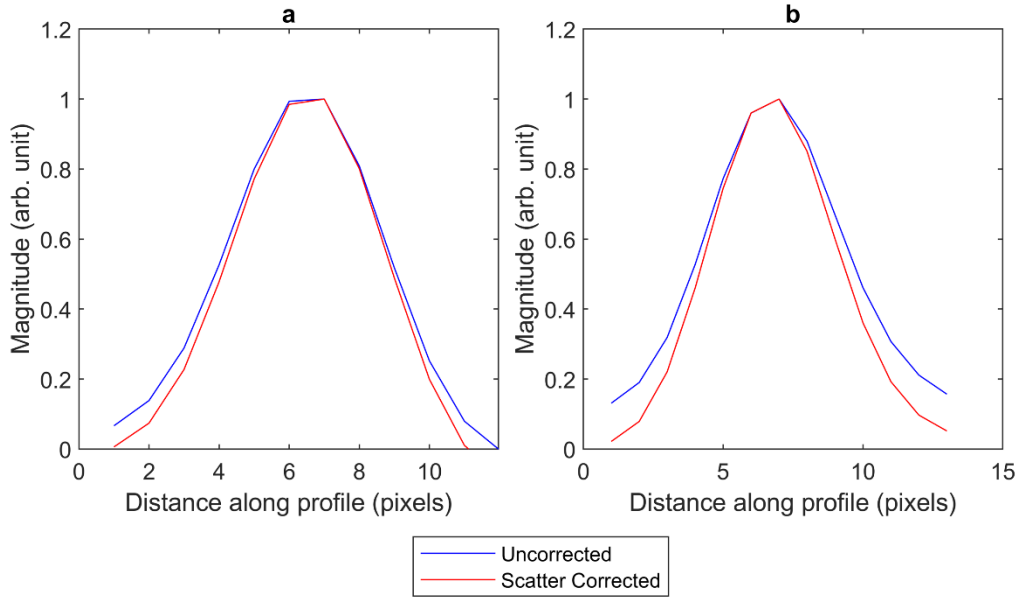

Figure 11: Comparison of line spread functions evaluated from the outer edge (a) and the inner edge (b) of the cobalt chrome cylinder before and after scatter correction.

4 Discussion and conclusions

A scatter correction method using a 2D focused anti-scatter grid has been demonstrated for 450 kV industrial XCT. The method leads to a 14.5% and 61.5% increase in CNR for a cobalt chrome sample and an Inconel sample respectively, and a 6% and 16.9% improvement in edge sharpness for outer and inner edges respectively. The method not only suppresses the scatter generated by the scanned object, but also considers the scattering of optical photons in the detector's scintillator. The proposed method requires two scans, one with the ASG and one without, alongside algorithmic correction of the projections prior to reconstruction.

The main disadvantage of the proposed method is the additional scan required, this may be prohibitive for high throughput production environments; however, the scan time is still likely to be significantly lower than equivalent fan-beam scan times. In future work we could investigate using a reduced number of projections for the scan with the ASG, this assumes that the change in scatter is small from one projection to the next, we expect this to be true for components with a simple geometry, but perhaps not for components with a more complex geometry. Another approach could be to leave the ASG in place and only conduct one scan, initial experiments showed that the ASG led to strong ring artefacts, this is due to the septa wall thickness being large (0.1 mm) in comparison to the detector pixel size (0.2 mm); thinner septa would reduce this, but thinner septa are also less effective at attenuating scatter. Using a grid artefact correction algorithm could be used to achieve scatter reduction in a single scan [15, 16, 17], most grid artefact correction strategies have been developed for radiography [12, 23], the requirements for tomography are more challenging because a high-pass filter is applied during reconstruction which emphases grid artefacts. Cobos et al. successfully managed to suppress 2D grid artefacts for tomography by implementing a multi-point detector gain and offset correction in combination with a Fourier domain filter that specifically targeted the frequency of the ASG [16, 17], albeit at clinical X-ray energies (80 kV).

Other factors that may influence the performance of the proposed method include: X-ray focal spot drift throughout a scan, this may lead to the projections from two scans being misaligned; errors in the homing of the rotation stage could also lead to projections from the two scans being misaligned by an angular offset; the shadow of the scanned object could be "burnt" into the scintillator after long scans, this could cause errors in the magnitude and shape of the scatter estimate. These errors can be minimised though applying good practice: warming up the X-ray source before commencing a scan, using high quality rotation stages with precise encoders, checking the condition of the detector and refreshing the gain and offset corrections if necessary (without changing the scan settings).

Comparing the proposed scatter correction approach to a beam stop approach, the main advantage of the proposed approach is the high spatial sampling of the scatter signal that is achieved in a single additional measurement. The beam stop approach requires multiple shifted measurements to be conducted to achieve high spatial sampling of the scatter signal. Simply using more stops or holes in a single array will block too much of the sample. Thus, the proposed approach overcomes the need for more than one additional scan.

The ASG used in this work was only 70 x 70 mm is size, whilst the detector is 400 x 400 mm. This is probative as only small components can be scanned. The small size of the ASG is due to limitations imposed by the ASG manufacturing process. Metal additive manufacturing systems with a larger build area exist, but they may not be able to fabricate such thin septa; hence, fabricating a 2D focused ASG that can cover a 400 x 400 mm flat panel detector is an open engineering challenge.

In conclusion, a 2D focussed ASG can reduce scatter and improve the CNR and edge sharpness of XCT data, however, the approach requires an additional scan.

5 Refences

[1] BS EN 16016-2:2011, Non destructive testing. Radiation methods. Computed tomography - Principle, equipment and samples, British Standards Institute, 2011.

[2] K. Schörner, Development of methods for scatter artifact correction in industrial X-ray cone-beam computed tomography, PhD Thesis, Technical University of Munich, 2012.

[3] G. Bucky, Method of and apparatus for projecting Röntgen images, US Patent 1164987A, 1915.

[4] G. Jarry, S. A. Graham, D. J. Moseley, D. J. Jaffray, J. H. Siewerdsen, F. Verhaegen, Characterization of scattered radiation in kV CBCT images using Monte Carlo simulations. Med. Phys., vol 33, no. 11, pp. 4320-4329, 2006.

[5] H. Ingleby, J. Lippuner, D. W. Rickey, Y. Li, I. Elbakri, Fast analytical scatter estimation using graphics processing units, Journal of x-ray science and technology, vol. 23, no. 2, pp. 119-133, 2015.

[6] N. Bhatia, D. Tisseur, F. Buyens, J. M. Létang, Scattering correction using continuously thickness-adapted kernels, NDT & E International, vol 78, pp. 52-60, 2016.

[7] N. Sakaltras, A. Pena, C. Martinez, et al., A novel beam stopper-based approach for scatter correction in digital planar radiography, Scientific Reports, vol. 13, no. 8795, 2023.

[8] L. Zhu, N. R. Bennett and R. Fahrig, Scatter Correction Method for X-Ray CT Using Primary Modulation: Theory and Preliminary Results, IEEE Transactions on Medical Imaging, vol. 25, no. 12, pp. 1573-1587, 2006.

[9] J. Maier, S. Sawall, M. Knaup, M. Kachelrieß, Deep scatter estimation (DSE): Accurate real-time scatter estimation for X-ray CT using a deep convolutional neural network, Journal of Nondestructive Evaluation, vol. 37, no. 57, 2018.

[10] K. Schörner, M. Goldammer, J. Stephan, Comparison between beam-stop and beam-hole array scatter correction techniques for industrial X-ray cone-beam CT, Nuclear Instruments and Methods in Physics Research Section B: Beam Interactions with Materials and Atoms, vol. 269, no. 3, pp. 292-299, 2011.

[11] H. Yan, X. Mou, S. Tang, Q. Xu, Improved scatter correction in X-ray cone beam CT with moving beam stop array using Johns' equation, Proceedings of the 10th International Meeting on Fully Three-dimensional Image Reconstruction in Radiology and Nuclear Medicine, Beijing, China, 2009.

[12] D. Jeon, H. Cho, H. Lee, H. Lim, M. Park, W. Youn, A software-based method for eliminating grid artifacts of a crisscrossed grid by mixed-norm and group-sparsity regularization in digital radiography, Nuclear Instruments and Methods in Physics Research Section A: Accelerators, Spectrometers, Detectors and Associated Equipment, vol. 1025, 2022.

[13] T. Alexeev, B. Kavanagh, M. Miften, C. Altunbas, Two-dimensional antiscatter grid: A novel scatter rejection device for Cone-beam computed tomography. Medical physics, vol. 45, no. 2, pp. 529–534, 2018.

[14] C. Altunbas, B. Kavanagh, T. Alexeev, M. Miften, Transmission characteristics of a two dimensional antiscatter grid prototype for CBCT, Medical physics, vol. 44, no. 8, pp. 3952–3964, 2017.

[15] C. Altunbas, Y. Park, Z. Yu, A. Gopal, A unified scatter rejection and correction method for cone beam computed tomography, Medical physics, vol. 48, no. 3, pp. 1211–1225, 2021.

[16] S. F. Cobos, H. N. Nikolov, S. I. Pollmann, D. W. Holdsworth, Reduction of ring artifacts caused by 2D anti-scatter grids in flat-panel CBCT, Proc. SPIE 11312, Medical Imaging 2020: Physics of Medical Imaging, 1131228 (16 March 2020); https://doi.org/10.1117/12.2548778

[17] S.F. Cobos, C. J. Norley, H. N. Nikolov, D. W. Holdsworth, 3D-printed large-area focused grid for scatter reduction in cone-beam CT, Medical Physics, vol. 50, pp. 240–258, 2023.

[18] W. J. Liu, C. Fan, Design and testing of an anti-scattering grid for medium-energy X-ray flash radiography, Applied Radiation and Isotopes, vol. 107, pp. 24-28, 2016.

[19] S. A. Watson, M. Appleby, J. Klinger, S. Balzer, C. Lebeda, D. Bowman, J. Montoya, D. Bultman, C. Vecere, C. Gossein, Design, fabrication and testing of a large anti scatter grid for megavolt γ-ray imaging, 2005 IEEE Nuclear Science Symposium Conference Record, Fajardo, PR, USA.

[20] D. Lazos, J. F. Williamson, Impact of flat panel-imager veiling glare on scatter-estimation accuracy and image quality of a commercial on-board cone-beam CT imaging system, Medical Physics, vol. 39, pp. 5639-5651, 2012.

[21] C. Schneider, W. Rasband, K. Eliceiri, NIH Image to ImageJ: 25 years of image analysis, Nature Methods, vol. 9, pp. 671–675, 2012.

[22] ASTM E1441-11 Standard Guide for Computed Tomography (CT) Imaging, ASTM International, West Conshohocken, PA, 2011.

[23] R. Rana, A. Jain, A. Shankar, D. Bednarek, S. Rudin, Scatter estimation and removal of anti-scatter grid-line artifacts from anthropomorphic head phantom images taken with a high resolution image detector, Fifty-seventh annual meeting of the American association of physicists in medicine, Anaheim, 2015.

6 Acknowledgements

This research was supported by A*STAR under its Industry Alignment Fund-Pre Positioning, grant number A20F9a0045. Any opinions, findings and conclusions or recommendations expressed in this material are those of the authors and do not reflect the views of A*STAR.